

QUASI-ONE-DIMENSIONAL ORGANIC CONDUCTORS IN HIGH MAGNETIC FIELDS

J.S. BROOKS

*NHMFL/Physics, Florida State University, Tallahassee FL 32310 USA
E-mail: brooks@magnet.fsu.edu*

O.H. CHUNG

*Department of Physics, Suncheon University, Suncheon, Chunnam 540-742 South Korea
E-mail: ohchung@suncheon.ac.kr*

We review the mechanisms and physical properties of quasi-one-dimensional (Q1D) conductors in high magnetic fields. Low dimensional materials are susceptible to instabilities which lead to broken symmetry ground states, including charge density wave, spin density wave, and superconductivity. Since the characteristic temperatures of phase transitions are often relatively low, the corresponding magnetic fields where profound changes in their ground states can occur are within the range of accessible dc and pulsed magnetic fields. We focus on more recent work and on Q1D systems that are not yet well known in the popular literature.

1 Introduction

Electronically anisotropic, quasi-one-dimensional (Q1D) organic materials in the charge transfer class, together with their many ground states, have been the subject of active study for more than 20 years, especially since the discovery of superconductivity in $(\text{TMTSF})_2\text{PF}_6$ by Jerome and co-workers¹. Quite often, the discovery of superconductivity somehow “anoints” a new material as interesting and worthy of further study. The superconducting ground state tells us that many body effects are important, and that other phenomena or ground states may be in close proximity. These are generally accessible with a little push with pressure, chemistry, or magnetic field. This grows even more interesting in highly anisotropic materials, where the the electronic states may become physically confined in one or more directions. Indeed, it was pressure that induced superconductivity in the otherwise insulating spin density wave (SDW) ground state of $(\text{TMTSF})_2\text{PF}_6$, which at ambient pressure results from a Q1D instability. The importance of high magnetic fields came closely on the heels of this discovery since the nature of the critical field is necessary to describe the essential details of superconductivity: coherence length, penetration depth, H_{c1} , H_{c2} for the vortex lattice, and H_{Pauli} for the field carefully aligned in-plane for these low dimensional materials. But, superconductivity was only the beginning of the story, since high magnetic fields revealed a new world of low dimensional physics, primarily due to the close proximity of Zeeman, orbital (either closed or transverse), electronic (imperfect nesting - see below), and transition temperature energy scales.^a There is a vast literature on low-dimensional organic metals, which is very thoroughly treated in the undisputed classic book by Ishiguro, Yamaji, and Saito². Since it would be futile to try to repeat the material in this as in other

^aFor a typical Q1D organic metal with a density wave transition of order 12 K (T_{DW}), at 30 T (easily obtained at any modern high field laboratory) these energies are $\mu_B H = 1.74$ meV, $\hbar\omega_c = 3.5$ meV, $\hbar\omega_b = 4.5$ meV, $t'_b = 0.5$ meV, $T_{\text{DW}} = 1.0$ meV.

Table 1: Transfer integrals and possible low temperature ground states for representative Q1D compounds (parameters from Ref. ²). Here *a*, *b* and *c* refer to the principal crystallographic axes.

	(TMTSF) ₂ PF ₆	(TMTTF) ₂ X	(Per) ₂ M(mnt) ₂	(DMET-TSeF) ₂ AuCl ₂
<i>t_x</i> (meV)	300 (a)	250(a)	150 (b)	420 (a)
<i>t_y</i> (meV)	25 (b)	10(b)	2(a)	64(b)
<i>t_z</i> (meV)	1 (c)	1 (c)	0 (c)	-
ground states	SDW, SC, FISDW	CL, SP, SDW	CDW	SC, FISDW

major reviews^{3–6}, we will try to focus only on those issues and phenomena that are most relevant to Q1D in high magnetic fields. We will focus on several distinctly different Q1D systems that have been the subject of high magnetic fields, and which also test different aspects of our understanding of the physics of Q1D materials. Useful formulae relevant to the understanding and analysis of the properties of Q1D materials in magnetic fields will likewise be presented.

2 Electronic Structure of Quasi-One-Dimensional Materials

In Fig. 1, we have tried to capture the main aspects of the Q1D scenario. Q1D conductors are really three-dimensional materials, it is just that the bandwidth between molecules within the conducting chains (*t_a*) is much larger than that between the chains (*t_b*), which, in turn, is larger than that between the (really two-dimensional) layers consisting of parallel chains (*t_c*). In Table 1, the transfer integrals for a representative group of materials to be discussed in this report and their possible ground states are shown.^b

From the transfer integrals, the tight binding model leads to a simplified dispersion relation

$$\epsilon(\vec{k}) = -2t_a \cos(ak_x) - 2t_b \cos(bk_y) - 2t_c \cos(ck_z) \quad (1)$$

where *a*, *b*, and *c* are lattice parameters along the *x*, *y*, and *z*-axis, respectively.^c In the case of Q1D anisotropy where we neglect the inter-layer bandwidth *t_c*, this reduces to (after Hasegawa and Fukuyama⁷)

$$\epsilon(\vec{k}) = v_x(|k_x| - k_F) - 2t_b \cos(bk_y) + 2t'_b \cos(2bk_y) \quad (2)$$

where

$$v_x = \frac{2at_a}{\hbar \sin(ak_F)} \quad \text{and} \quad t'_b = \frac{t_b^2 \cos(ak_F)}{4t_a \sin^2(ak_F)}. \quad (3)$$

^bIt is worth noting that for bulk crystals, the molecular and lattice vibrational modes always have three-dimensional degrees of freedom.

^cIn many Q1D materials, the *a*, *b*, and *c* axes refer to the intrachain (*x*), interchain (*y*), and interplane (*z*) directions, and we will generally follow this convention. Likewise, the unit cell axes may not be normal to the crystallographic planes (*b'*, *c'*, etc.) but we will use the *a*, *b*, and *c* notation for simplicity with this understanding.

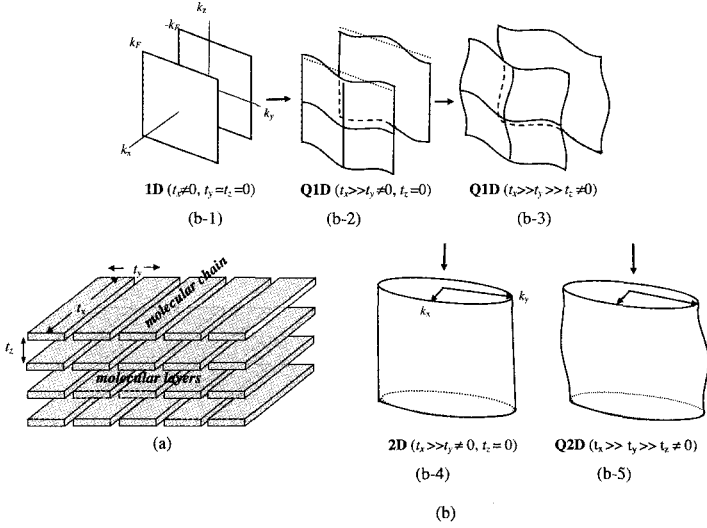


Figure 1: (a) Schematic representation of a typical quasi-one-dimensional crystal structure. (b) Evolution of the Fermi surface for various combinations of transfer integrals (t_x, t_y , and t_z) for 1D and 2D systems.

The Fermi surface (FS) is then described by

$$k_x = \pm(k_F + (2t_b \cos(bk_y) - 2t'_b \cos(2bk_y))/\hbar v_x) . \quad (4)$$

The term t'_b above is called the imperfect nesting parameter. If we neglect it in Eq. (4), the resulting FS will be two purely sinusoidal sheets at $\pm k_F$ as shown in Fig. 2. By transposing the $-k_F$ sheet by a factor of $2k_F$ to $+k_F$, and shifting it up by π/b , the two FS sheets will exactly overlap. This is called perfect nesting and the vector of transposition is the perfect nesting vector $\vec{Q}_0 = (2k_F, \pi/b)$. As discussed below, this will lead to a fully gapped system at the Fermi level. However, when t'_b increases, then higher order terms appear in the dispersion and it is not possible for \vec{Q}_0 to gap all the FS. Eventually, for $t'_b = k_B T_{\text{SDW}}$, the nesting will be too small to stabilize a density wave state. This is depicted in Fig. 2 where the dependence of the reduced ordering temperature is shown vs. the variation of the imperfect nesting parameter. The inset curves are the $+k_F$ sections of the $\vec{Q} = (2k_F, \pi/b)$ nested FS for $t_a = 250$ meV, and t_b for the range 10, 15, 20, and 24 meV, where t'_b is computed from Eq. (3) above for a T_{SDW} of 12 K.^d Here t'_{b0} corresponds to the critical imperfect nesting factor for stabilizing a spin density wave(SDW) phase at 0 K and evaluated as $T_{\text{SDW}}^0/1.13$ where T_{SDW}^0 is the temperature for perfect nesting (e.g. $t'_b = 0$). Electron and hole pockets arise as a result of imperfect nesting. As Fig. 2 shows, the changes in Fermi surface topology due to the degree of imperfect nesting which can destroy the SDW phase are very small, compared with the b -axis bandwidth.

^dThe values for an actual material will depend on the band filling, nesting vector, etc.

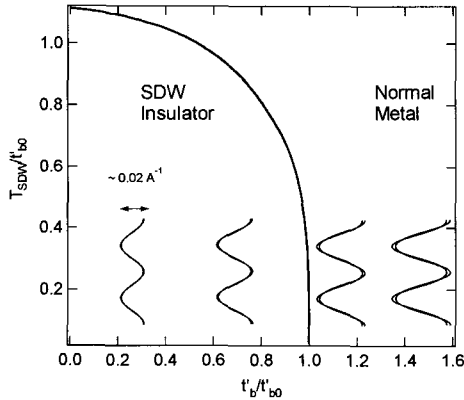


Figure 2: Stability of a SDW ground state versus the imperfect nesting parameter t'_b/t'_{b0} . Nested FS sheets (for $+k_F$ only) are shown for increasing t_b for $t_a = 250$ meV and $m^* = 1.0 m_0$ following Eqs. (1)-(4) (see text for details).

3 The Effect of High Magnetic Fields on Q1D Systems

The primary mechanism by which the magnetic field interacts with a Q1D is through Zeeman and orbital coupling. The Zeeman term, which acts on the π electron system, will always be present. The relationships between the nesting vectors and the spin-split bands are shown in Fig. 3 for both the spin density wave (SDW) and charge density wave (CDW) pairing states for a simple 1D band configuration. In CDW systems, the field acting through the Pauli susceptibility, will destroy (in the absence of orbital coupling) the CDW ground state. However, for a SDW system⁸, the optimum nesting vector does not change as the bands split. For a superconducting ground state, if the field is carefully aligned in the conducting plane of a material with negligible interplane coupling $t_z \sim 0$, the vortex lattice is suppressed, and the superconducting ground state will be governed only by Pauli or other non-vortex mechanisms.

In the normal state, the orbital coupling is through the Lorentz force $\hbar \partial \vec{k} / \partial t = e \vec{v}_k \times \vec{B}$, where the electron dynamics in magnetic field are obtained through the Landau-Peierls substitution $\vec{k} \rightarrow \vec{k} - e \vec{A} / \hbar$. In a Q1D picture, $\vec{A} = (0, H_x, 0)$ is generally used in the Landau gauge. Orbital effects depend on the degree to which the material deviates from a strictly one-dimensional chain, as shown for different relative transfer integral values in Fig. 1(b). For $t_x \neq 0, t_y = t_z = 0$ in our notation, there are only two parallel Fermi surface sheets (Fig. 1(b-1)), the electron motion is strictly confined to each single chain, and the magnetic field has no orbital effect. For $t_x \gg t_y \neq 0, t_z = 0$, the real space electron orbit will move along the chains with oscillatory spatial motion in the y direction (Fig. 1(b-2)) due to the Lorentz force. Here, an electron with Fermi velocity v_F along the x -direction in the presence of a magnetic field will cross the Brillouin zone in the y -direction with frequency $\omega_b = ev_F H b / \hbar$ as depicted in Fig. 4(a). The amplitude of the y motion will decrease with increasing magnetic field, thereby, driving the oscillatory motion more one-

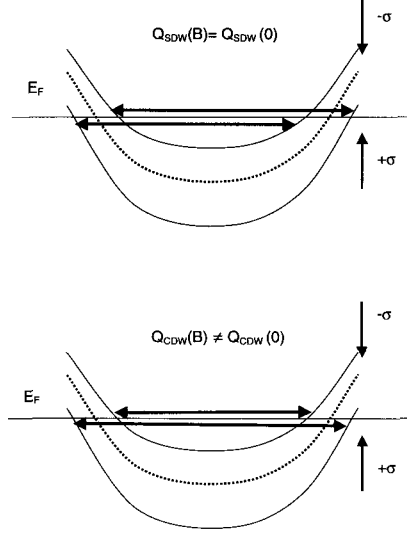


Figure 3: Scenarios for nesting at the Fermi surface for finite magnetic field. Dashed lines represent the zero magnetic field bands, where the nesting vector in both cases is just $2k_F$. (a) For SDW nesting with $\sigma_{\uparrow} \sigma_{\downarrow}$ electron-hole pairing, the nesting vector does not change from $Q_{SDW}(0) = 2k_F$ with increasing field. (b) For CDW nesting with $\sigma_{\uparrow} \sigma_{\uparrow}$ and $\sigma_{\downarrow} \sigma_{\downarrow}$ electron-hole pairing, the nesting vectors increase (decrease) from $Q_{CDW}(0) = 2k_F$ continuously with increasing field.

dimensional. Chaikin has given an intuitive description which describes this process³. This approach yields the real-space amplitude $A_y = 4bt_b/\hbar\omega_b$ and wavelength $\lambda_x = h/eHb$ of the real-space motion of a carrier in the direction of the conducting chains (see Fig. 4).

We note that, not until a field of order 1000 T is reached, will the carrier be confined within a single chain. However, for a metallic Q1D system, a field of order 10 T (where A_y and λ_x are still much larger than the lattice constants) is sufficient to induce a SDW state. A detailed description of how CDW and SDW ground states emerge in a Q1D system, and, moreover, how a magnetic field can induce a SDW ground state⁹ is beyond the scope of this report. However, we can summarize the essential features as follows: Both the CDW and SDW ground states are the result of a rearrangement of the charge, spin, and lattice parameters to lower the free energy of the Q1D system. For low on-site repulsion $U \ll t_a$, a CDW is favored, but when the on-site repulsion is stronger ($U \approx t_a$), a SDW is favored. As shown in Fig. 3, a characteristic nesting vector of order $2k_F$ connects opposite Fermi surface sheets, and for any perturbation at this wave number the instability will arise. Theoretically, when the computed generalized susceptibility $\chi(\vec{Q})$ diverges for a particular value of \vec{Q} , this is an indication of an instability for that nesting vector. The divergence decreases as the dimensionality of the system increases. In $(\text{TMTSF})_2\text{ClO}_4$ at low temperatures, the imperfect nesting is too large for a SDW state to develop, and the optimum nesting vector $\vec{Q} = (2k_F, \pi/b)$ cannot produce a gap. However, in finite field a new component of the k_x wave vector, $\kappa = eHb/\hbar$, (i.e., $2\pi/\lambda$ as given above) arises. Indeed,

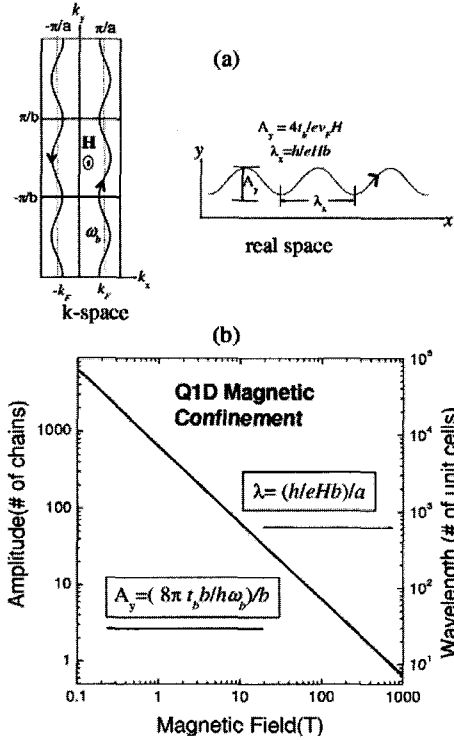


Figure 4: (a) Semiclassical motion of Q1D electrons in k -space and real space in the presence of a magnetic field (after Ref. ³). (b) Variation of the electron orbital amplitude (in the inter-chain direction) and wavelength (along the chains) with magnetic field $H \parallel z$.

when $\vec{Q} = (2k_F + \kappa n, \pi/b)$, where n is an integer, $\chi(\vec{Q})$ can exhibit singularities, and the SDW can be stabilized, leading to a field induced SDW (FISDW) state. In the simple language of the Q1D Fermi surface topology, if the nesting is bad for $\vec{Q} = (2k_F, \pi/b)$, then if one shifts the nested sheet a bit more in the k_x direction by κn , part of the FS can be well nested. The second, and equally important part of this process is that the un-nested sections of the FS will produce closed pockets with quantized area $2\pi eH/\hbar$. When the spin and orbital energies are considered, this configuration, which leads to a FISDW state, is the lowest energy ground state⁹. Since κ increases linearly with field, this also leads to quantum cascade features in the FISDW. The Fermi level stays in between the Landau levels of the pockets (the energy is lowered by having all Landau levels filled below E_F), and this gives rise to a quantum Hall effect^{10–13}.

For $t_x \gg t_y \gg t_z \neq 0$ (Fig. 1(b-3)), the oscillatory motion can occur as well along the z -axis. In this case, geometric resonance effects can arise for magnetic field tilted along certain crystallographic directions, leading to magic angle effects. For Q1D metals,

a commensurate effect of the electron motion between b - and c -directions is observable at magic angles in magnetoresistance in tilted fields in the bc -plane, as Lebed pointed out first¹⁴. The condition for Lebed oscillations in triclinic structure, an evidence of the Q1D system, is given by the condition

$$\tan(\theta) = \frac{p}{q} \cdot \frac{b \sin \gamma}{c \sin \beta \sin \alpha} - \cot \alpha^* \quad (5)$$

where p and q are integers and b, c, α, β , and γ are lattice parameters of the crystal. As can be seen from Eq. (5), the physical information from the AMRO effect in Q1D system is purely related to the geometry of crystal structure and not to topology of 1D bands (Fig. 6). If the y dispersion is sufficiently large to close the Fermi surface, or, if crystallographic ordering effects or nesting fold the Q1D Fermi surface, then cyclotron orbits due to electron and hole pockets can arise, and the system becomes quasi-two-dimensional (Q2D) as depicted in Fig. 1 (b-4) and (b-5). As will be more fully discussed in Sec. 3.4 below, quantum oscillations associated with the de Haas-van Alphen effect will occur, and in tilted magnetic fields Q2D resonances associated with the warped Q2D Fermi surface (Yamaji-Kajita-Kartsovnik effects^{15,16}) can be observed.

All of the above are called as the semi-classical Boltzmann transport effects. More exotic possibilities for electronic transport will be discussed in a subsequent section. But let's first discuss the basic phenomena in magneto-transport in real Q1D systems, where unless otherwise specified, we assume the field is perpendicular to the most conducting molecular plane.

3.1 A Simple Q1D Metal in High Magnetic Fields

We begin our exposition of Q1D materials in high fields with the $(\text{DMET-TSeF})_2\text{AuCl}_2$ class of materials¹⁷. These are characterized by their asymmetric donor character and their linear anion structure, AuCl_2 , AuI_2 (superconducting), AuBr_2 , or I_3 (no FISDW). Since no anion ordering occurs in these materials, the Fermi surface at low temperatures retains the simple open topology of a Q1D FS as depicted in Fig. 1(b). Hence, in principle, these materials should capture the essential aspects of a Q1D metal in high magnetic fields.

An example of the magnetic field dependent properties¹⁸ of $(\text{DMET-TSeF})_2\text{AuCl}_2$ is shown in Fig. 5. Although in a strictly 1D system there is no magnetoresistance for finite interchain bandwidth, a slightly superlinear MR is generally observed. At higher magnetic fields a series of features appear, which are field-induced spin density wave (FISDW) transitions. These are the result of the orbital confinement mechanism^{9,19} which drives the system towards 1D instabilities. Here, a quantized FISDW gap opens over part of the Fermi surface, and the resistance rises. Superimposed on the FISDW structure is the appearance of so-called rapid oscillations. The frequencies of these oscillations are generally in the range of 200 T. Although not universally accepted, we believe that the rapid oscillations are the result of Q2D pockets that result from a reconstructed Q1D Fermi surface, either by anion ordering (see Fig. 7 below), or by field induced nesting (see Fig. 3). To our knowledge, rapid oscillations have never been observed in an open orbit, strict Q1D system without nesting or reconstruction.

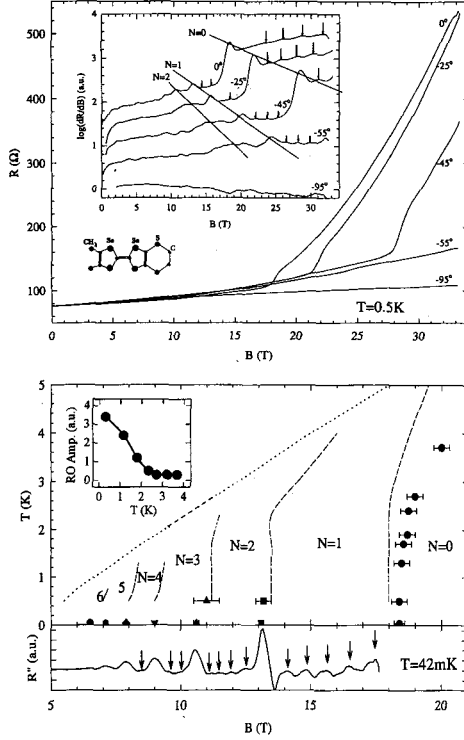


Figure 5: Magnetic field dependence of the asymmetric system $(\text{DMET-TSeF})\text{AuI}_2$ (after Ref. ¹⁸). Upper panel: Angular dependent magnetoresistance (MR) study of the FISDW behavior. Inset: log-derivative of the MR showing the rapid oscillation (RO) and FISDW details. Lower panel: SDW temperature-magnetic field phase diagram for $\theta = 0$. Dashed lines are for the corresponding SDW phases in $(\text{TMTSF})_2\text{PF}_6$. Lower inset shows the second derivative of the MR and the RO behavior. Upper inset indicates the temperature dependence of the RO amplitudes, which increase monotonically with lower temperatures.

As the magnetic field is tilted into the conducting planes of the material, the positions of the FISDW and RO positions follow a $1/\cos(\theta)$ dependence, which is characteristic of a Q2D orbital system. Deviations from this behavior have been observed in the FISDW state, and have been attributed to a sliding of the FISDW state in tilted magnetic fields. The temperature dependence of the rapid oscillations in the $(\text{DMET-TSeF})_2\text{AuCl}_2$ system monotonically increases with lower temperatures, which is characteristic of a Q2D quantum oscillation amplitude. As noted below, the temperature dependence becomes more complicated in other Q1D materials with SDW ground states. The angular dependent magnetoresistance (AMRO) for several of the $(\text{DMET-TSeF})_2\text{X}$ systems ²⁰ is shown in Fig. 6. This phenomenon, known as the “Lebed” effect, follows the behavior described above for Eq. (5). Here features in the magnetoresistance for a constant magnetic field vs. angular rotation in the plane perpendicular to the conducting chains reveal structure for field directions that

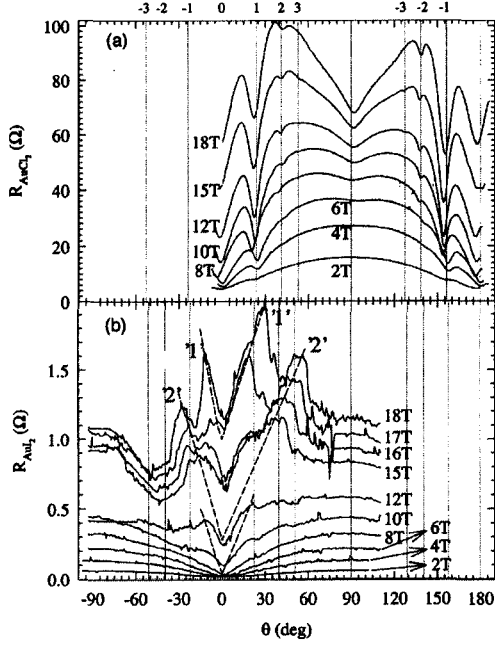


Figure 6: Angular dependent magnetoresistance effects in $(\text{DMET-TSeF})_2\text{X}$ for $\text{X} = \text{AuCl}_2$ (upper panel) and $\text{X} = \text{AuL}_2$ (lower panel) for different magnetic fields. θ is the angle of the magnetic field from the b -axis. Vertical lines represent the Lebed angles calculated from the lattice parameters and labelled as p/q according to Eq. (5). Numbers in quotes indicate the FISDW index corresponding to each maxima. Broken lines are guides for the eye for the shift of these maxima (after Ref. ²⁰).

involve integer ratios of the lattice constants in the y and z directions. This type of behavior is specific to Q1D systems. As discussed below, for a Q2D system, the relevant parameter is the product of the interplane lattice constant z and the Fermi momentum k_F .

In summary of this section, the DMET class of materials give a simple description of Q1D physics in high fields where complications due to anion ordering are not present.

3.2 A Q1D Metal with Fermi Surface Reconstruction

Q1D systems, where anion ordering can occur, will cause doubling of the unit cell in one or more directions, resulting in a reconstruction of the Fermi surface. Q1D $(\text{TMTSF})_2\text{X}$ materials with low symmetric tetrahedral anions such as ClO_4 , ReO_4 , and FSO_3 will generally undergo anion ordering below a characteristic temperature T_{AO} , which for $(\text{TMTSF})_2\text{ClO}_4$ is 24 K. Although randomly oriented at room temperature, the tetrahedral anions order in an up, down, up, down arrangement, and this doubles the unit cell along the b -axis direction, resulting in a new reciprocal lattice $(k_a, k_b/2, k_c)$ or more simply $(0, \frac{1}{2}, 0)$ as depicted in the bottom of Fig. 7 (as will be discussed in Sec. 3.4, the reconstruction can be modified

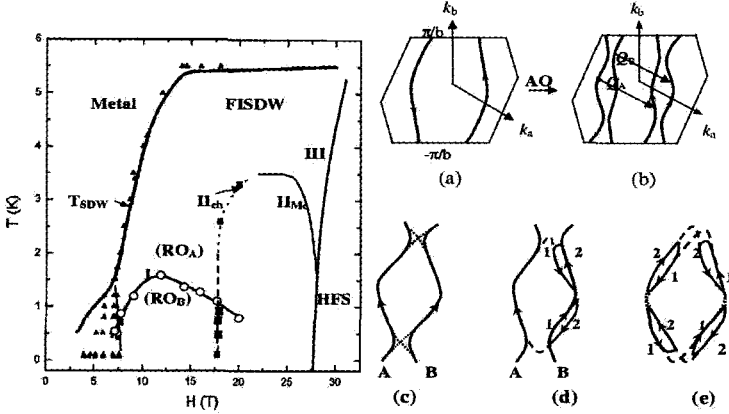


Figure 7: Left: Detailed picture of the FISDW phases for $(\text{TMTSF})_2\text{ClO}_4$ **I**: $T^*(H)$ by Chung *et al.*²⁶ **II**_{Mc}: McKernan's 3.5 K phase boundary in the FISDW state²¹. The main metal-to-FISDW phase boundary is shown by TSDW, where at low temperatures a cascade of transitions are seen below 8 K. At higher fields below TSDW new phase boundaries appear due to the complexity of the nesting phenomena, as determined from the RO behavior and other anomalies in the magnetoresistance: **II**_{ch}: low field side extension of **II**_{Mc} **III**: High field state boundary. Bottom: (a) FS of a normal Q1D metal. (b) FS of metallic state with AO along the b' -axis. Here Q_A and Q_B are two possible SDW nesting vectors. (c) The Stark interference oscillation between two parallel electron motions. (d) Coexistence of SDW_A nesting with Q_A and metallic FS. (e) Small electron and hole pockets are formed after both SDW nestings occur.

by pressure). This results in “folding” the Fermi surface sheets inwards in the reduced zone scheme Fig. 7(b). Since there are now four Q1D Fermi surface sheets, the magnetotransport behavior becomes more complicated.

It is important to note that for anion ordering, the cooling rate is of enormous importance. For $(\text{TMTSF})_2\text{ClO}_4$, a cooling rate of a few mK per minute through the 24 K transition is sufficient to produce a well ordered ground state, which is metallic and superconducting. However, as the cooling rate is increased, there will be systematically more disorder in the material, and this can lead to additional, complicated behavior in the magnetotransport phenomena²². In an extreme case where $(\text{TMTSF})_2\text{ClO}_4$ is thermally quenched (Q- ClO_4), there is no anion ordering, the simple Q1D FS remains, and a SDW state occurs below 5 K (see Sec. 3.3). A rapid oscillation (RO) frequency is observed in the SDW state with a frequency of 190 T²³. In $(\text{TMTSF})_2\text{PF}_6$, where there is also no anion ordering and a SDW below 12 K, Ulmet and co-workers²⁴ first discovered RO with a frequency of about 220 T. In these latter two cases, the RO amplitudes are non-monotonic in temperature, with a maximum in the range 1 to 3 K below T_{SDW} . The RO behavior in the case of $(\text{TMTSF})_2\text{ClO}_4$ is very complicated, as treated in study of $(\text{TMTSF})_2\text{ClO}_4$ by Uji *et al.*²⁵ and Chung *et al.*²⁶, as depicted in Fig. 8. Unlike the situation for $(\text{DMET-TSeF})_2\text{AuCl}_2$ above with no FS reconstruction, quantum oscillations with frequency $F \simeq 260$ T are observed in the metallic phase of $(\text{TMTSF})_2\text{ClO}_4$ outside the FISDW transition. Based on the reconstructed Fermi surface topology due to anion ordering as shown in Fig. 7(b), these oscillations are thought

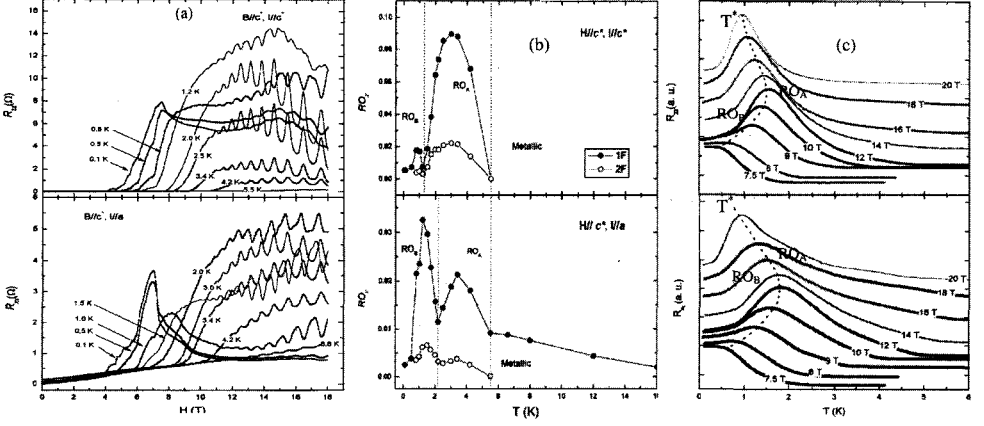


Figure 8: Behavior of rapid oscillations for in-plane ($I \parallel a$) and inter-plane ($I \parallel c^*$) transport in well relaxed $(\text{TMTSF})_2\text{ClO}_4$. (a) Rapid oscillations in the magnetoresistance for different temperatures. Note that there are two different oscillatory components that appear in the MR behavior, RO_A and RO_B . (b) Non-monotonic temperature dependence of the RO_A and RO_B oscillation amplitudes. (c) Temperature dependence of magnetoresistance in fixed fields. T^* refers to the peak in the MR versus T for different fields (after Ref. ²⁶).

to arise from Stark interference between adjacent orbits ²⁷. They are not thermodynamic, are not seen in magnetization, and do not occur in the strictly Q1D $(\text{TMTSF})_2\text{PF}_6$ and Q- ClO_4 systems. Hence in Fig. 7 the FS reconstruction shown by anion ordering along the b -axis is necessary to produce the Stark mechanism.

Inside the FISDW phase, rapid oscillations of the same frequency are seen, but here the behavior is more complex, with two distinct types of oscillations present (RO_A and RO_B as shown in Fig. 8). Since anion ordering produces four Q1D sheets, the field induced nesting is more complicated. As illustrated in Fig. 8(b), as temperature falls below a characteristic temperature T^* , the rapid oscillation changes in behavior (the temperature and field dependence of their amplitude, and shape and phase by ϕ of the oscillations are different). Correspondingly, the temperature dependence of the magnetoresistance changes (the magnetoresistance is maximum at the T^* in Fig. 8(c)). A possible scenario is that two separate SDW nestings with different wave vectors (\vec{Q}_A and \vec{Q}_B) between two pairs of sheets take place at different temperature regime and then result in two types of the oscillations with the same frequency. The temperature dependence of the Stark and the RO amplitudes are given in Fig. 8(b). While the Stark amplitudes increase at low temperatures, the RO amplitudes in the FISDW phase have a non-monotonic dependence on temperature. It is worth noting that for all materials with a SDW ground state at zero field (i.e. $(\text{TMTSF})_2X$ ($X = \text{PF}_6, \text{AsF}_6, \text{NO}_3$, and Q- ClO_4), the RO amplitudes are observed to increase below T_{SDW} until about 2 K, after which they rapidly (exponentially) decrease to zero ²³. In contrast, for the $(\text{DMET-TSeF})_2\text{AuCl}_2$ system, there are no Stark oscillations since there

is no reconstruction of the Q1D FS at zero field. Also, the RO oscillations in the FISDW state are observed to increase monotonically as discussed above (see Fig. 5).

At even higher magnetic fields ($H \geq 28$ T), new effects arise in the $(\text{TMTSF})_2\text{ClO}_4$ material. The rapid oscillations were investigated up to 50 T in the high field state in pulsed magnetic fields²⁸, as shown in Fig. 9. The high field state is expected to be the $n = 0$ nested state by the “standard model”⁹ rather than reentrant metallic phase. Recalling the field dependent nesting vector $2k_F + n\kappa$ discussed in Sec. 3, for $n = 0$, at high fields the system is expected to recover the optimal nesting vector configuration $(2k_F, \pi/b, 0)$. In high field state, only a single type of the ROs has been observed for a broad temperature range. The temperature dependence of the RO amplitude increases monotonically with decreasing temperature down to 0.3 K but the field dependence changes around 2 K. Interestingly, the frequency of the rapid oscillations ($F_1 = 260$ T) remains the same regardless of where in the $(\text{TMTSF})_2\text{ClO}_4$ phase diagram the RO are observed. However, characteristics of the oscillations such as temperature and field dependence of the amplitudes are distinct. A unified picture of the origin of the RO phenomena for the full field and temperature range is not yet forthcoming. We note that there are theoretical predictions for an oscillation of the Metal-FISDW phase boundary T_{FISDW} in high magnetic fields²⁹. Recently Radic, Bjelis, and Zanchi have treated this general problem theoretically³⁰, where they predict both the RO and the FISDW phase diagram, including a prediction of oscillations in the T_{FISDW} phase boundary. However, to our knowledge, this has not yet been observed.

3.3 Field Dependence of Q1D SDW and CDW Ground States

3.3.1 The SDW ground state in high magnetic fields

An overview of nesting scenarios for SDW and CDW ground states in magnetic field are shown in Fig. 3. Here, the Zeeman energy removes the degeneracy of the band at the Fermi level. In the simple pairing model, high magnetic fields do not destroy the SDW ground state — when the band is spin split, the nesting vector does not change significantly since the pairing is between the σ_{\uparrow} and σ_{\downarrow} bands. Moreover, when the nesting of the SDW is imperfect, the transition temperature will increase with magnetic field towards the perfect nesting value. This is due to orbital confinement effects that drive the system into a more perfectly nested state^{31,32}. An overview of these effects is given in Fig. 10 for a number of materials in the Bechgaard salts²³. The zero field SDW transition temperature decreases as the degree of imperfect nesting increases, as can be seen for $(\text{TMTSF})_2\text{PF}_6$, $(\text{TMTSF})_2\text{NO}_3$, Q- $(\text{TMTSF})_2\text{ClO}_4$, and finally highly ordered (relaxed) R- $(\text{TMTSF})_2\text{ClO}_4$ where the zero field ground state is superconducting, and only in high fields is a FISDW state induced.

To complete our discussion of the $(\text{TMTSF})_2\text{ClO}_4$ system in very high fields we briefly discuss a measurement where flux compression was used to explore the very high field MR of a Q- ClO_4 sample by Mielke *et al.*³³. To our knowledge, this is the highest field to which transport in a single organic conductor crystal has been successfully studied. As shown in Fig. 11, a significant increase in resistance is observed as the field enters the SDW phase at about 20 T at 8 K (see phase diagram of Q- ClO_4 in Fig. 10). In the lower panel their oscillatory signal, obtained by subtracting the background, clearly shows the RO

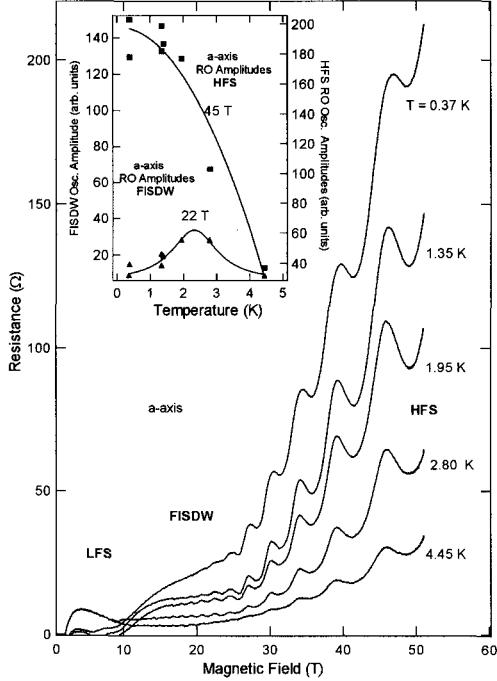


Figure 9: Magnetoresistance and oscillatory component of a well-ordered $(\text{TMTSF})_2\text{ClO}_4$ sample at the University of New South Wales Pulsed Magnet Laboratory. In the FSDW phase, the RO amplitudes have a non-monotonic dependence on temperature, but in the high field state (HFS) the RO amplitudes grow with decreasing temperature (after Ref. ²⁸).

signal. Although the data is somewhat uncertain, the frequency is in the range of 190 T, comparable to non-destructive pulsed field measurements on Q-ClO_4 .

3.3.2 The CDW ground state in high magnetic fields

For a pre-existing CDW ground state, T_{CDW} will decrease with magnetic field due to the Pauli-limit of the CDW ground state ⁸,

$$T_{\text{CDW}}(H) = T_{\text{CDW}}(0) - \frac{\gamma\mu_B^2}{4k^2T_{\text{CDW}}(0)}. \quad (6)$$

With reference to Fig. 3b, the CDW state is systematically removed as the nesting condition which requires $Q = Q_{\text{CDW}}(0)$ degrades. Since $T_{\text{CDW}}(0)$ is generally of order 100 K for most materials, very high fields are needed to suppress the CDW ground state. The reduction of T_{CDW} by a magnetic field was first demonstrated in TTF-TCNQ by Tiedje and co-workers ³⁴, where a slight, but measurable suppression of the CDW state was observed. The CDW system $(\text{Per})_2\text{M}(\text{mnt})_2$ (where Per = perylene, mnt = maleonitriledithiolate and M = Au and Pt) has a much lower T_{CDW} (~ 10 K). Here, work by Almeida and co-workers showed

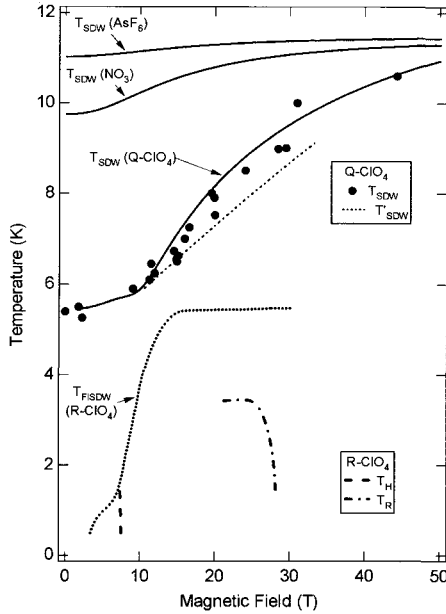


Figure 10: Temperature vs. magnetic field dependence of the SDW phase diagram of Q-ClO₄. Here the simple Q1D FS remains since the AO transition is suppressed. A SDW phase develops at zero field below 5 K. The magnetic field dependence of the SDW phases are shown in terms of the theoretical expression of Bjelis and Maki (solid lines) with the parameters v_F , T_0 , and ε_0 for $X = \text{AsF}_6$ ($v_F = 2.4 \cdot 10^5$ m/s; $\varepsilon_0 = 7$ K; $T_0 = 11.5$ K), $X = \text{NO}_3$ ($v_F = 2.4 \cdot 10^5$ m/s; $\varepsilon_0 = 13$ K; $T_0 = 11.0$ K), and $X = \text{Q-ClO}_4$ ($v_F = 1.1 \cdot 10^5$ m/s; $\varepsilon_0 = 22.5$ K; $T_0 = 13.0$ K). The dashed line is a polynomial fit to $T_{\text{SDW}2}$ vs. $B_{\text{SDW}2}$, which was a second feature observed in the pulsed field MR data. Note: For each material, the label is in the respective metallic phase region, and the lower temperature, higher field region beyond the phase boundary is the SDW phase. (See Ref. ²³ for discussion.)

a reduction of T_{CDW} by about 20 % at 18 T. Recent higher field studies ^{35,36} clearly show the suppression of the CDW state by 30 T, and at even higher magnetic fields a second, field induced CDW (FICDW) is observed. The mechanism for the FICDW is at present not fully understood, but it seems to involve both spin and orbital coupling, as described recently by Zanchi, Bjelis, and Montambaux ³⁷, and may also depend on multiple Q1D bands at the Fermi level ^{36,38}. We note that it is also theoretically feasible to realize a field induced CDW, starting from an imperfectly nested ground state, as treated by Lebed ¹⁴, Fujita *et al.* ³⁹, and also Zanchi *et al.* ³⁷. However, experiments to date have only involved the magnetic field alteration of systems with zero field CDW states.

3.4 Q1D Systems under Pressure and in Magnetic Fields - A Special Case

In general, hydrostatic pressure will increase the tight binding bandwidths, and in particular the interchain bandwidth t_y . This increases the imperfect nesting parameter, and generally

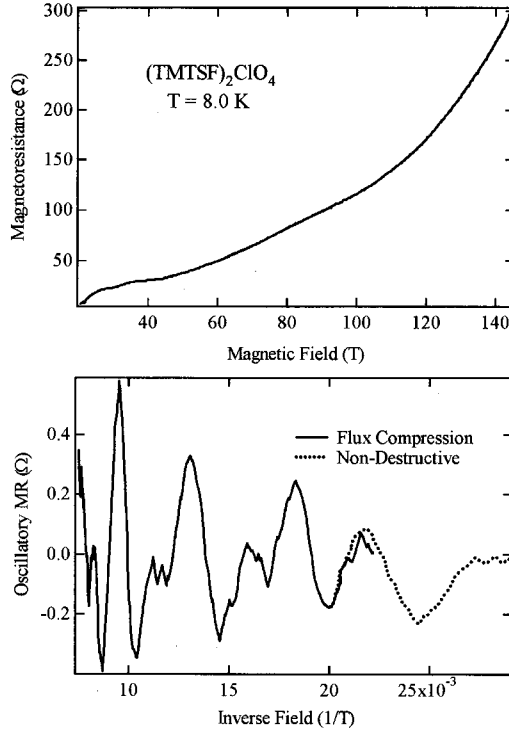


Figure 11: Magnetoresistance and oscillatory component of a Q-(TMTSF)₂ClO₄ sample in a flux compression-type destructive magnet at 8 K. The second overlapping trace at lower fields in the oscillatory data is from a non-destructive pulse. The Fourier transform gives a RO frequency in the range of 190 T, in accord with more extensive non-destructive measurements for Q-(TMTSF)₂ClO₄. Referring back to Fig. 10, a temperature of 8 K corresponds to a threshold field of 20 T, which is consistent with the rapid rise in resistance seen in the flux-compression data (after Ref. ³³).

induces a metallic, and as we noted in the introduction for (TMTSF)₂PF₆, even a superconducting ground state. However, in high magnetic fields the magnetic orbital confinement can again reduce the effective interchain coupling, and re-stabilize a Q1D nested ground state. The interplay of these mechanisms with pressure and high magnetic field has been beautifully demonstrated in (TMTSF)₂PF₆ by Kang *et al.*, and we refer the reader to that work ⁴⁰, since this is now a well-known story.

To put a new light on pressure effects in Q1D systems, we consider the work by Chung and co-workers ⁴¹ who have recently been investigating the effect of on the (TMTSF)₂FSO₃ salt. The FSO₃ anions have a tetrahedral structure (like ClO₄ and ReO₄) but contain permanent electric dipole moment due to the asymmetric electronegativity from two kinds of atoms (F and O) at the four apices. Therefore, extra features in (TMTSF)₂FSO₃ related to the electric dipole moment may offer an additional degree of freedom to the system.

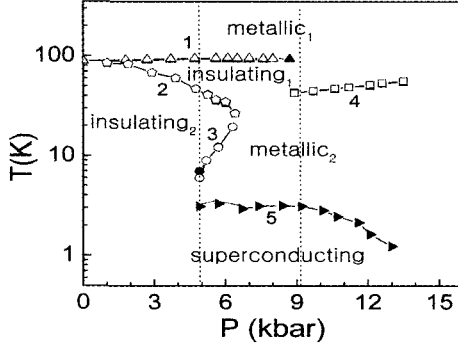


Figure 12: A refined P - T phase diagram of $(\text{TMTSF})_2\text{FSO}_3$ from temperature dependent resistance measurements for fixed pressures (after Ref. ⁴¹).

Early investigations of 1980's⁴²⁻⁴⁴ showed that at ambient pressure $(\text{TMTSF})_2\text{FSO}_3$ undergoes a metal-insulator transition due to anion ordering with a wave vector $\vec{Q} = (\frac{1}{2}, \frac{1}{2}, \frac{1}{2})$ at ~ 90 K⁴⁵. The pressure-temperature phase diagram for $(\text{TMTSF})_2\text{FSO}_3$ is shown in Fig. 12. It is well known that $\vec{Q} = (\frac{1}{2}, \frac{1}{2}, \frac{1}{2})$ anion ordering induces a MI transition for TMTSF salts such as $(\text{TMTSF})_2\text{ReO}_4$ and $(\text{TMTSF})_2\text{BF}_4$ ^{46,45}. For $(\text{TMTSF})_2\text{FSO}_3$, as pressure above ~ 5 kbar is applied, superconductivity appears below 3 K, which is the highest transition temperature yet observed in the Bechgaard salts. In the initial study, it was somewhat surprising that the pressure-temperature phase diagram seemed rather simple, with a monotonic field dependence of magnetoresistance, and there was no indication of additional features due to the electric dipole moment of FSO_3 anions. However, recent measurements of interlayer resistance and longitudinal thermodynamic power revealed a rich phase diagram of $(\text{TMTSF})_2\text{FSO}_3$ as shown in Fig. 12.

Briefly reviewing the phase diagram in Fig. 12, the ~ 90 K M-I transition (1) at zero pressure splits into two transitions as pressure is applied. The upper transition temperature is relatively independent of pressure whereas the second transition (2) rapidly decreases. Above 4.8 bar, a metallic phase reappears below 20 K (3), and then a superconducting transition (5) takes place at around 3 K. It is very unusual to have two successive transitions and reentrance to the metallic state after the system has undergone $(\frac{1}{2}, \frac{1}{2}, \frac{1}{2})$ ordering. However, the superconducting state is not complete since the resistance does not reach zero at low temperature. At pressures greater than 9 kbar, while T_c decreases very rapidly with pressure ($dT_c/dP \approx 0.5$ K/kbar compared with ≈ 0.09 K/kbar for $(\text{TMTSF})_2\text{PF}_6$), a new phase transition (4) appears at ~ 35 K. For many Bechgaard salts, the application of pressure is necessary to observe superconductivity, but a further increase of the pressure results in a decrease of T_c . Decrease of T_c with the pressure itself is nothing unusual and can be explained with the simple BCS model of conventional superconductors. Although its origin is not clarified yet, it is possible that a new kind of anion ordering may occur as another anion ordering with $(0, \frac{1}{2}, \frac{1}{2})$ dominates at pressures above 8 kbar in the ReO_4 salt^{47,48}. Details for phase characteristics are described in Ref. ⁴¹.

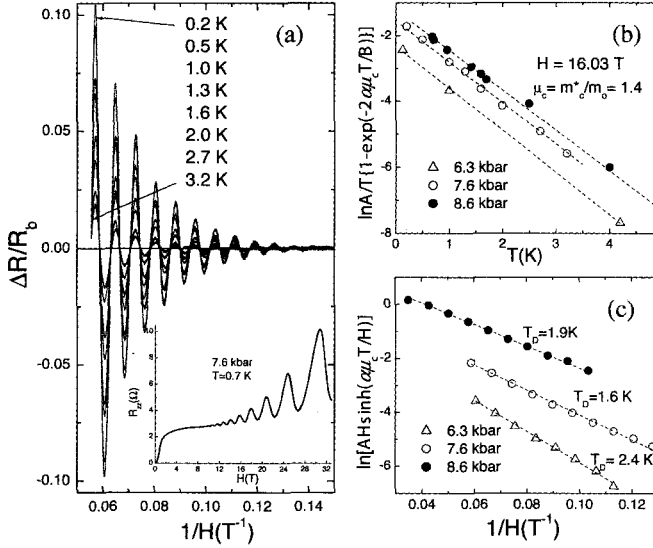


Figure 13: $(\text{TMTSF})_2\text{FSO}_3$ quantum oscillatory signals analyzed in terms of the LK Q2D formalism. (a) SdH oscillations at various T for $(\text{TMTSF})_2\text{FSO}_3$ at 6 kbar. (b) The effective mass m_c and (c) Dingle temperature T_D is obtained from the 2D Lifshitz-Kosevich equation (after Ref. ⁴⁹).

More exceptional features have been discovered when high fields were applied to the $(\text{TMTSF})_2\text{FSO}_3$ salt under pressure, in particular in the intermediate range ($5 < P < 9$ kbar), the optimal condition for the superconductivity. As a magnetic field is applied along the c^* -axis, a single series of oscillations with the primary frequency $F_0 = (130 \pm 1)$ T (as opposed to rapid oscillations - see below) appear above 5 T as shown in the inset of Fig. 13 from Ref. ⁴⁹. As described below, the oscillation features are quite different from those of ROs. First of all, no field induced phase transitions appear at least up to 33 T even with the zero field superconducting ground state. The absence of the FISDW phases in the presence of superconductivity is quite exceptional in the $(\text{TMTSF})_2\text{X}$ salts. This is counter to Yakovenko's suggestion ⁵⁰ that the same pairing interaction gives rise to superconductivity at zero fields and to the FISDW under magnetic field in the Q1D Bechgaard salts (the $(\text{DMET-TSeF})_2\text{AuCl}_2$ series described in Sec. 3.1 above also do not follow the Yakovenko description). The oscillation features are quite different from the ROs in most of Bechgaard salts, the lowest frequency (only 130 T as compared to 260 T in $(\text{TMTSF})_2\text{ClO}_4$) and monotonic increase of the oscillation amplitude with decreasing temperature and increasing field as illustrated in Fig. 13. This is a typical behavior for the closed orbits on the Fermi surface, in contrast to the scenario of the RO's for other $(\text{TMTSF})_2\text{X}$ salts as discussed in Sec. 3.2. The cross sectional area in the ab' -plane is estimated as $1.25 \cdot 10^{14} \text{ cm}^{-2}$ from $F = (\hbar/4\pi^2e)S$, which corresponds to 1.6 % of the area of the first Brillouin zone ($S_{\text{FBZ}} = 7.5 \cdot 10^{15} \text{ cm}^{-2}$) using the lattice parameters given by Ref. ⁴². We may apply the Lifshitz-Kosevich (L-K) formula ⁵¹ since the oscillation behavior implies a closed orbital motion of the electrons. The oscillation amplitude in the L-K

formula can be represented as:

$$\frac{\Delta R}{R_0} = A_0 \frac{\alpha T e^{-\alpha m_c / m_0 T_D / H}}{H^q \sinh(\alpha m_c / m_0 T / H)} \sum \cos(2\pi(N \frac{F}{H} - \gamma)) \quad (7)$$

where $\alpha = 2\pi^2 k_B m_0 / e \hbar = 14.69$ T/K, T_D is the Dingle temperature, m_c is the effective mass, and m_0 is the free electron mass. The power q of H in Eq. (7) depends on the dimensionality of the closed motion. For the SdH amplitude in the 2D model q is equal to 1 whereas $q = \frac{1}{2}$ in 3D⁵¹. The data are well fitted to the 2D L-K formula, as shown in Fig. 13, supporting the existence of the 2D closed FS in the (TMTSF)₂FSO₃ Bechgaard salt. The L-K analysis yields an effective mass and Dingle temperature of $m_c = (1.4 \pm 0.05)m_0$ and $T_D = 1.6$ to 2.5 K, respectively. The absence of frequency beating indicates that the FS has no detectable warping along the k_z direction.

The true, two-dimensional nature of the Fermi surface in the (TMTSF)₂FSO₃ salt under pressure is further revealed by angular dependent magnetoresistance studies. Strikingly, angular magnetoresistance oscillations (AMRO) do not follow the Lebed-type resonance feature as observed in most Bechgaard salts⁵²(see Sec. 3 above). On the other hand, for 2D bands with a corrugated cylindrical Fermi surface, as a tilted magnetic field approaches to special angles (periodic in $\tan \theta$) the electron energies near Fermi surface are fully quantized into Landau levels, resulting in the enhancement of magnetoresistance¹⁵. As the AMRO of (TMTSF)₂FSO₃ are Yamaji oscillations as illustrated in Fig. 14, the FS of (TMTSF)₂FSO₃ is indeed a corrugated 2D FS. To properly compare the area of the 2D FS from AMRO to that obtained from the SdH frequency, a complete Fermi surface topology must be constructed from the AMRO periods observed for each polar angle θ rotation about an axis defined by the azimuthal angle ϕ , as described by the relationship¹⁶

$$\tan \theta_N = \frac{\pi}{c k_{\parallel}(\phi)} (N - \frac{1}{4}) + C(\phi) . \quad (8)$$

Here, c is the distance between adjacent conducting planes, k_{\parallel} is the average Fermi wave vector parallel to the major axis, N is the index of resonance, and θ_N is the angle for the N -th peak from the cylindrical axis. $C(\phi)$ is a function of azimuthal angle. The Fermi wave vector k_{\parallel} can be readily determined from the slope of the $\tan \theta_N$ versus N plot in Eq. (8). Fig. 14(a) and (b) is angular magnetoresistance of (TMTSF)₂FSO₃ under 7.2 kbar, at 1.5 K in 24 T for several azimuthal angles (bottom) and plot of $|\tan \theta_N|$ versus N , respectively.

As shown in Fig. 14(b), the slope is different at different ϕ , meaning k_F is anisotropic in the ab -plane. Using a geometrical construction⁵³, the value of the Fermi momentum $k_F(\phi)$ is determined from the wave vector $k_{\parallel}(\phi)$. Amazingly, as shown in Fig. 15(a), a lens-shaped closed orbit in the ab -plane is thereby derived, where $k_F^b \approx 1.4 \cdot 10^7$ cm⁻¹ and $k_F^a \approx 0.35 \cdot 10^7$ cm⁻¹. From the computed cross sectional area, we find $S = 1.25 \cdot 10^{14}$ cm⁻² in good agreement with that derived from the SdH frequency. More important information for the Q2D Fermi surface of (TMTSF)₂FSO₃ is obtained by the coherent peak of width 4.0° for $H \parallel b'$ as marked with circle in Fig. 14(a), indicating the existence of the third directional warping of the cylindrical Fermi surface, introduced by Hanasaki *et al.*⁵⁴. From

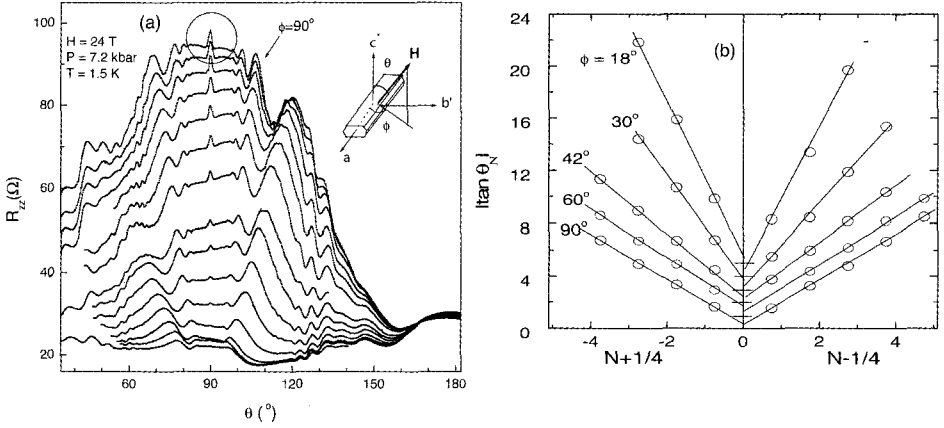


Figure 14: Angular magnetoresistance oscillations in $b'c^*$ -plane rotation in $(\text{TMTSF})_2\text{FSO}_3$ (left). In addition to Yamaji oscillations the coherence peak (width $\sim 2^\circ$) is observed at $H \parallel b'$. The angular positions of the magnetoresistance peaks are well fit to Yamaji formula (right). (a) Angular magnetoresistance at $\phi = 90, 76, 72, 66, 60, 54, 48, 40, 36, 24, 18, 12, 6$ and 0° from the a -axis from top to bottom. (b) The slopes of $|\tan \theta_N|$ versus N at different ϕ show the Fermi surface on the ab -plane is anisotropic closed orbit.

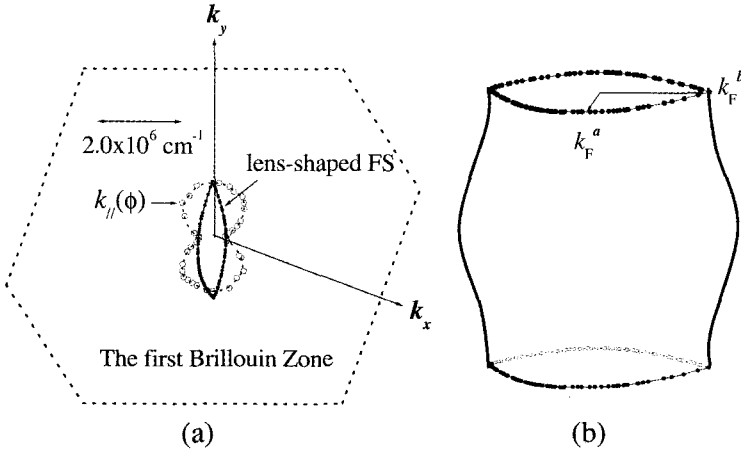


Figure 15: The warped cylindrical Fermi surface with lens shaped cross section in the ab -plane obtained from the AMRO measurements. The first Brillouin zone is shown for comparison, to scale. Lower panel, AMRO data representation of the Q2D tube (not to scale). Note that the coherence peak in Fig. 14 is most pronounced for the field along the b -axis direction, where the FS curvature of the warped FS should be the greatest.

the half width of this peak the transfer integral along the c -direction can be obtained by

$$\frac{\pi}{2} - \theta_c = \frac{2m_c t_c c}{\hbar^2 k_F} \quad (9)$$

where θ_c is the half width of coherence peak angle. Using the values of m_c and k_F obtained from the SdH oscillations above, t_c is estimated as ~ 1.0 meV, comparable with that of $(\text{TMTSF})_2\text{ClO}_4$.

Here, we briefly review how pressure affects Q1D organic materials. In $(\text{TMTSF})_2\text{PF}_6$ salts, imperfect nesting parameter (t'_b) increases with hydrostatic pressure and then SDW insulating phase at zero pressure is suppressed and superconductivity appears. However, the one-dimensionality is not actually lost by pressure, as indicated by the FIDSW transitions and Lebed oscillations. In the $(\text{TMTSF})_2\text{ReO}_4$ salt, common Q1D features such as FIDSW and Lebed effects are also observed under pressures higher than 8 kbar with anion ordering with $(0, \frac{1}{2}, \frac{1}{2})$ induced by pressure. However, in $(\text{TMTSF})_2\text{FSO}_3$ salt pressure ($5 \leq P \leq 11$ kbar) induces real two-dimensional electron motion. The lens shaped Fermi surface with sharp edges along the b' -axis indicates intersection between two warped FS sheets. The complete Fermi surface in $(\text{TMTSF})_2\text{FSO}_3$ is sketched in Fig. 15(b). Whether the mechanism of the two-dimensionality induced by pressure is possibly related to electric dipole moment of $(\text{TMTSF})_2\text{FSO}_3$ anions or is simply due to the pressure effect increasing interchain transfer integral t_b (or both) is not clear at this point.

3.4.1 *Uniaxial compression studies of Q1D materials - a mystery?*

As depicted in Fig. 2, the difference between the SDW and metallic ground states in Q1D systems, for instance $(\text{TMTSF})_2\text{PF}_6$, are very sensitive to the imperfect nesting parameter t'_b , which is related to the square of interchain bandwidth t_b . Since a hydrostatic pressure of 6 kbar completely removes the SDW in $(\text{TMTSF})_2\text{PF}_6$, we expected that the SDW ground state would be even more rapidly suppressed with uniaxial compression along the b -axis of a $(\text{TMTSF})_2\text{PF}_6$ crystal. When the experiments were carried out, we were surprised by the insensitivity of the SDW ground state in $(\text{TMTSF})_2\text{PF}_6$ to uniaxial compression. Two types of uniaxial compression experiments were involved. The first was the Maesato-method⁵⁵ where the sample is encapsulated in an epoxy cylinder, and then pressurized at room temperature in a standard clamp cell. It is believed that this method provides a truly uniaxial strain since the walls of the clamp suppress the Poisson expansion. The variation of T_{SDW} with uniaxial strain is shown for $(\text{TMTSF})_2\text{PF}_6$ in Fig. 16 for all three crystallographic directions. Estimates based on the pressure dependence of the resistivity anisotropy indicated that for b -axis strain, t'_b/t_a increased by almost 50 % i.e. 10 kbar⁵⁶.

The effects of uniaxial stress on the SDW state of $(\text{TMTSF})_2\text{PF}_6$ have been independently studied by our group both at zero field⁵⁷ and in high fields (presented in this section) to determine the stress dependence of T_{SDW} and Δ_{SDW} . In these experiments a Poisson effect is present since there are no confining walls in the piston-anvil arrangement, but there is an advantage since the stress can be increased in situ at cryogenic temperatures during a high field magnet experiment by the Campos method^{58,59}. Systematic studies were carried out for uniaxial strain for the three different crystal directions for magnetic fields applied

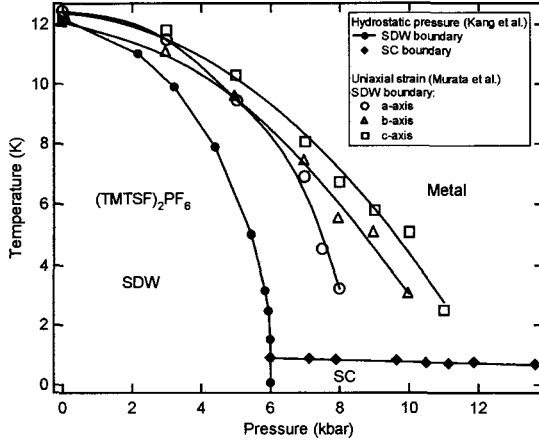


Figure 16: T_{SDW} versus uniaxial strain along the three axes of $(TMTSF)_2PF_6$ (after Ref. ⁵⁶). Shown for comparison is the corresponding phase diagram for $(TMTSF)_2PF_6$ with hydrostatic pressure (after Ref. ⁴⁰).

along the c -axis and current along the a -axis. Changes in the electronic structure were monitored by analyzing the frequency of the rapid oscillation frequency, as shown in Figs. 17, 18 and 19, where different aspects of the experiment are presented. For the a - and b -axes measurements, a transverse method was employed to apply stress⁶⁰ with a vertical field along the c -axis, whereas for the c -axis data the stress could be directly applied vertically. For good mechanical coupling, the stress induced strong reductions in the resistance. Hence, in Fig. 17 it is possible that the transverse coupling was insufficient for some reason, at least below 8.5 kbar, since the MR decreases by only a factor of two. Although there are large uncertainties, the RO frequency appears to decrease with a -axis stress. The most important direction for nesting is for b -axis stress, as shown in Fig. 18. Here, we find a reduction of the MR by almost two orders of magnitude, and above 4 kbar a significant increase in the RO frequency, where we note that between 0 and finite stress, the RO frequency first decreases, and then increases monotonically (for b and c -axis stress). As in previous studies, the SDW ground state is still present at 8.5 kbar, and even for b -axis stress, the imperfect nesting parameter must still be below its critical value. In Fig. 19 the c -axis stress reduces the resistance by 10 kbar, nearly three orders of magnitude. The RO amplitudes were small, but clearly observed by background subtraction as shown for 6 kbar. The RO frequency showed a marked monotonic increase after the initial drop between 0 and 0.5 kbar.

Since pressure suppresses the SDW phase, the large changes in resistance are in part due to closing a gap, and to a lesser extent due to the increase in bandwidth. Hence the simple golden rule argument where $t_i^2 \approx \sigma_i$ ($i = a, b, c$) is not a reliable measure of changes in, for instance, t_b . Changes in the RO frequency therefore provide a more reliable measure of the effects of stress, since they are due to changes in the Fermi surface topology. If we focus on the b - and c -axes data, we find that the electronic structure changes by about 5 % between 5 and 8.5 kbar and by 12 % between 1 and 10 kbar respectively. Under the assumption

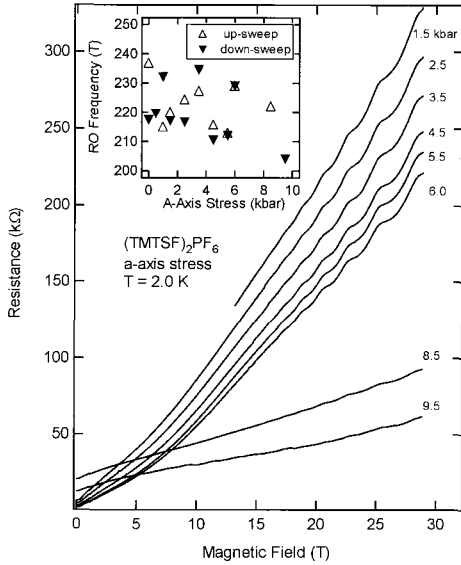


Figure 17: *a*-axis uniaxial stress dependence of the magnetoresistance and rapid oscillation frequency (inset) of $(\text{TMTSF})_2\text{PF}_6$ at 2.0 K.

that the RO arise from closed pockets in a nested FS, these pockets are increasing in both cases, i.e. the imperfect nesting is increasing. But referring back to Fig. 2, this increase is small, and it is not able to remove the SDW state, even by 10 kbar of uniaxial stress. In zero field studies where uniaxial stress was applied directly along each axis⁵⁷ (without the transverse coupling uncertainty), T_{SDW} and Δ_{SDW} were remarkably insensitive to pressure. Recalling the uniaxial strain studies described above in Fig. 16, here too, the SDW state remained up to the highest pressure studied.

For completeness, we have checked the *b*-axis uniaxial stress for $(\text{TMTSF})_2\text{ClO}_4$, as shown in Fig. 20 at 4.2 K. We found that the RO frequency decreased significantly with the increasing *b*-axis stress, in contrast to the behavior of $(\text{TMTSF})_2\text{PF}_6$ in Fig. 18. Hence, it is clear that the details of the molecular structure (tetrahedral versus centro-symmetric anions for instance) play a significant role in the effects of uniaxial stress. In this regard, the motivation for the uniaxial studies was the expectation that compression along the *b*-axis of $(\text{TMTSF})_2\text{PF}_6$ would have a dramatic effect on the imperfect nesting parameter t'_b (since it is of order $1/50$ of t_b). However, for all three axes, at the highest uniaxial (stress or strain) pressures, well above the critical hydrostatic pressure where $(\text{TMTSF})_2\text{PF}_6$ becomes metallic and superconducting, the SDW still exists⁴⁰. The answer to this mystery may lie in the approximate description of the electronic structure as given in Eq. (1). The transfer integrals are actually averages of intermolecular interactions over multiple directions between donor sites⁶¹. In addition, uniaxial strain may involve molecular changes (sliding, bending) that are not along the stress direction, as reported in Q2D systems⁵⁹. It seems

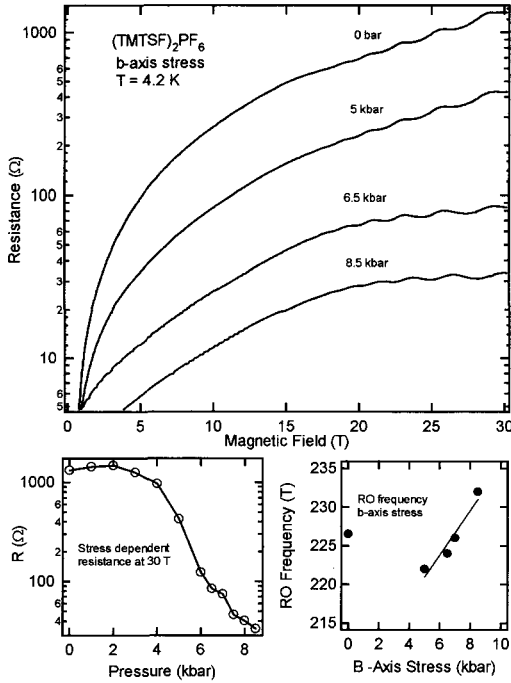


Figure 18: b -axis uniaxial stress dependence of the magnetoresistance (both in field and pressure at 30 T), and rapid oscillation frequency of $(\text{TMTSF})_2\text{PF}_6$ at 4.2 K.

evident that for hydrostatic pressure, the axial compression may be more uniform, leading to a more straightforward reduction in the effective t'_b .

4 Exotica in the Bechgaard Salts

There are several further studies of the $(\text{TMTSF})_2\text{X}$ system (primarily $(\text{TMTSF})_2\text{PF}_6$ under pressure) in high magnetic fields that should briefly be mentioned.

4.1 Non-Fermi Liquid Behavior and Magic Angles

The first involves the investigation of the angular dependent magnetoresistance versus crystallographic direction in a magnetic field range where the material is in the normal metallic state, and where the FISDW transitions are not observed. Both experimental⁵² and theoretical¹⁴ work indicated that at certain magic angles peaks or dips in the MR would occur associated with integer ratios of the b and c lattice parameters (as described above in Sec. 3 and Eq. (5)).

Subsequently Danner *et al.* discovered a set of oscillations⁶² associated with fields tilted near the a -axis, which allowed a determination of the t_b parameter. In general, these

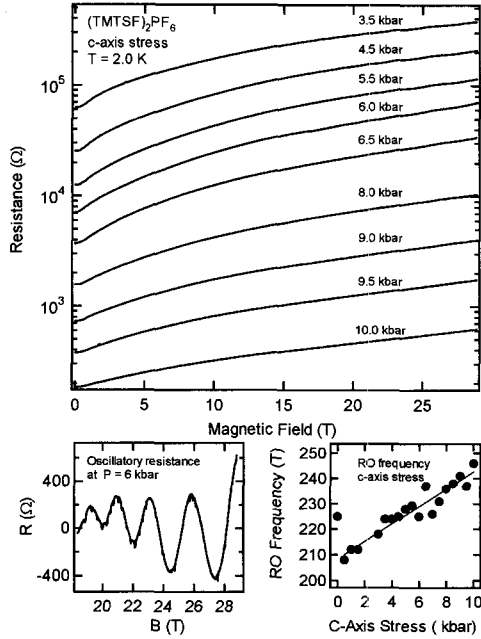


Figure 19: *c*-axis uniaxial stress dependence of the magnetoresistance (MR) and rapid oscillation (RO) frequency of $(\text{TMTSF})_2\text{PF}_6$ at 2.0 K. The RO amplitudes are apparent when the background MR is subtracted from the MR signal.

previous studies followed a semi-classical Boltzmann transport behavior. However, upon closer examination, it was found that the temperature dependent resistivity (and also the magnetic field dependence) showed a non-metallic behavior for magnetic field along certain directions, and from these studies, a non-Fermi liquid description has been proposed^{63,64,65}.

4.2 Unconventional Superconductivity

The sensitivity to disorder of the superconducting transition in $(\text{TMTSF})_2\text{ClO}_4$ gave an initial hint that the superconductivity might be unconventional. Further evidence for triplet superconductivity in $(\text{TMTSF})_2\text{PF}_6$ was advanced as the result of a series of experiments where the magnetic field is aligned in the *a*-*b* plane with very high precision⁶⁶. In this case, electrical transport measurements showed that the critical field in $(\text{TMTSF})_2\text{PF}_6$ exceeded the Pauli limit by as much as a factor of two or more⁶⁷. NMR studies^{69,68} that followed showed that there was no Knight shift below the superconducting transition, giving further support for triplet pairing. Very recently, measurements by both transport and magnetization⁷⁰ show that the critical field in $(\text{TMTSF})_2\text{ClO}_4$ for $B \parallel b$ exceeds the Pauli limit by at least a factor of two. Results for both $(\text{TMTSF})_2\text{PF}_6$ and $(\text{TMTSF})_2\text{ClO}_4$ are shown in Fig. 21.

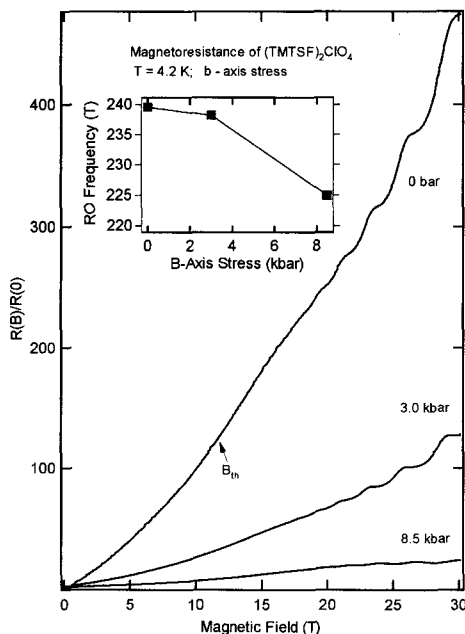


Figure 20: *b*-axis uniaxial stress dependence of the magnetoresistance and rapid oscillation frequency for (TMTSF)₂ClO₄ at 4.2 K. The FISDW transition threshold field is about 12 T at 4.2 K at zero pressure, but was not evident at higher pressures. Notably, unlike (TMTSF)₂PF₆, the RO frequency decreases with the increasing *b*-axis stress.

4.3 Quantum Hall Effect (Integer)

(TMTSF)₂PF₆, under pressure^{10,11}, exhibits a quantum Hall behavior in the cascade of FISDW transitions, as does (TMTSF)₂ReO₄¹². In some cases, the sign of the Hall signal will reverse¹³. The integer Hall effect is a result of the Fermi level residing in the Landau gap for each FISDW subphase, where the transitions occur when the nesting vector shifts from one quantum value to the next³. It is interesting to note that for the CDW system η -Mo₄O₁₁, there is also a well-defined integer Hall effect observed⁷¹. Hence, the presence of a SDW or CDW ground state with imperfectly nested FS sheets appears to be a desirable condition to observe integer Hall plateaus in bulk materials.

5 The Next Frontier in Organic Low Dimensional Materials

There will continue to be many fundamental discoveries in these materials which will result from a combination of more careful experiments, new types of measurements, higher magnetic fields and/or lower temperatures, and new compounds. One exciting prospect, suggested in the pulsed magnet and flux compression studies in Figs. 9 and 11, is to push the magnetic field of investigation well above 100 T with careful, well-characterized exper-

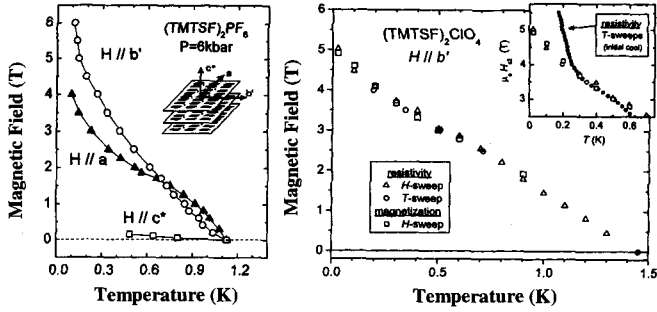


Figure 21: Left panel: critical field of $(\text{TMTSF})_2\text{PF}_6$ for $B \parallel b^*$ from transport studies (after Ref. ⁶⁷). Right panel: critical field of $(\text{TMTSF})_2\text{ClO}_4$ for $B \parallel b^*$ for both transport and magnetization measurements (after Ref. ⁷⁰).

iments. Then, in the spirit of Fig. 4, the magnetic lengths will truly start to approach the unit cell dimensions, and new physics should arise.

A second exciting prospect is to “go nano”. Physical confinement effects involving sample sizes that approach the characteristic SDW, CDW, and SC coherence lengths would also provide new insight into these low-D ground states. The challenge is to make high quality charge transfer complex structures in ultra-thin films and/or quantum dot configurations.

A third area, related to the second, is in the area of applications, and recent work has been reported on an organic FET made with the TMTSF donor system ⁷². However, mobilities of single component organic materials in FET configurations seem to be relatively low (of order $1 \text{ cm}^2/\text{Vs}$), and usually decrease with lower temperature. Rather, it might be useful to exploit truly epitaxial systems in the charge transfer complex configuration which would be very close to a density wave instability, and which could be easily switched with a modest electric field. Such a structure represents significant technical and synthetic chemistry challenges which will have to be met.

Finally, returning to the topic of the introduction, superconductivity has driven the quest for new organic materials. However, the superconducting transition for organic charge transfer salts has been stuck below 14 K for over 10 years. It may be that this represents a fundamental limit for T_c for these materials. Nevertheless, there is strong evidence that the superconductivity is unconventional, as discussed above, and that surprises await us when the right material is synthesized. Little’s model ^{74,75,2} for an excitonic superconductor, which has been one of the driving forces for the synthesis of new low-D superconductors, has not yet been realized. Hence, this very early proposal still remains a goal for organic superconductivity.

6 Summary

The central theme of this short review is that the seemingly one-dimensional conducting materials are in principle two-dimensional, (and ultimately three-dimensional) systems.

Pressure will tend to make them more two-dimensional, and magnetic field will tend to make them more one-dimensional. The ground states and physical properties of Q1D systems are very sensitive to the details of the primitive Q1D Fermi surface which may undergo reconstruction or nesting. Hence, many of the seemingly exotic properties of these systems may often be understood simply in terms of the Fermi surface topology.

Acknowledgments

The work at FSU is supported by NSF-DMR 0203532. The National High Magnetic Field Laboratory is supported by NSF Cooperative Agreement No. DMR-0084173, by the State of Florida, and by the DOE.

References

1. D. Jerome, *et al.*, *J. de Physique Lett. (Paris)* **41**, L95 (1980).
2. T. Ishiguro, K. Yamaji and G. Saito, *Organic Superconductors*, 2nd ed. (Springer-Verlag, Berlin, Heidelberg, New York, (1998).
3. P.M. Chaikin, *J. Physique I* **6**, 1875 (1996).
4. D. Jerome and H.J. Shultz, *Adv. Phys.* **31**, 299 (1982).
5. J.P. Pouget and S. Ravy, *J. Physique I* **6**, 1501 (1996).
6. C. Bourbonnais and D. Jerome, in *Advances in Synthetic Metals: Twenty Years of Progress in Science and Technology*, edited by P. Bernier, S. Lefrant and G. Bidan (Elsevier, Amsterdam, 1999), p. 206-261.
7. Y. Hasegawa and H. Fukuyama, *J. Phys. Soc. Jpn.* **55**, 3978 (1986).
8. W. Dieterich and P. Fulde, *Z. Phys.* **85**, 3732 (2000).
9. P.M. Chaikin, *Phys. Rev. B* **85**, 3732 (2000); M. Heritier, G. Montambaux, and P. Lederer, *J. de Physique Lett. (Paris)* **45**, L-943 (1984); K. Yamaji, *J. Phys. Soc. Jpn.* **54**, 1034 (1985); M. Ya Azbel, P. Bak and P.M. Chaikin, *Phys. Lett. A* **117**, 92 (1986); K. Maki, *Phys. Rev. B* **33**, 4826 (1986).
10. S.T. Hannahs *et al.*, *Phys. Rev. Lett.* **63**, 1988 (1989).
11. J.R. Cooper *et al.*, *Phys. Rev. Lett.* **63**, 1984 (1989).
12. W. Kang, J.R. Cooper and D. Jerome, *Phys. Rev. Lett.* **43**, 11467 (1991).
13. H. Cho and W. Kang, *Phys. Rev. Lett.* **59**, 9814 (1999).
14. A.G. Lebed, *JETP Lett.* **43**, 174 (1986); *Phys. Rev. Lett.* **63**, 1315 (1989).
15. K. Yamaji, *J. Phys. Soc. Jpn.* **58**, 1520 (1989).
16. M.V. Kartsovnik *et al.*, *J. Physique I* **2**, 89 (1991).
17. K. Oshima *et al.*, *Synthetic Metals* **70**, 861 (1995).
18. N. Biskup *et al.*, *Phys. Rev. B* **60**, R15005 (1999).
19. L.P. Gor'kov and A. Lebed, *J. de Physique Lett. (Paris)* **45**, L433 (1984).
20. N. Biskup *et al.*, *Phys. Rev. B* **62**, 21 (2000).
21. S.T. McKernan *et al.*, *Phys. Rev. Lett.* **75**, 1630 (1995).
22. C.C. Agosta *et al.*, in *High Magnetic Fields in the Physics of Semiconductors*, Ed. D. Heiman, (World Scientific 1995), p. 738.

23. J.S. Brooks *et al.*, *Phys. Rev. B* **59**, 2604 (1999).
24. J.P. Ulmet, A. Khmou and L. Bachere, *Synthetic Metals* **19**, 271 (1987).
25. S. Uji *et al.*, *Phys. Rev. B* **53**, 14399 (1996).
26. O.H. Chung *et al.*, *Phys. Rev. B* **61**, 11649 (2001).
27. R.W. Stark and C.B. Friedberg, *J. Low Temp. Phys.* **14**, 111 (1974).
28. J.S. Brooks *et al.*, *Phys. Rev. B* **53**, 14406 (1996).
29. T. Osada, S. Kagoshima and N. Miura, *Phys. Rev. Lett.* **69**, 1117 (1992).
30. D. Radic, A. Bjelis, and D. Zanchi, *cond-mat/0206466* (2002).
31. K. Maki, *Synthetic Metals* **55-57**, 2808 (1993).
32. A. Audouard and S. Askenazy, *Phys. Rev. Lett.* **52**, 700 (1995).
33. C.H. Mielke *et al.*, in *Proc. Phys. Phenomena in High Magn. Fields - III*, Tallahassee, FL, (1998) (World Scientific), p. 257-260.
34. T. Tiedje *et al.*, *Can. J. of Phys.* **53**, 1593 (1975).
35. D. Graf *et al.*, *Phys. Rev. B* **69**, 125113 (2004).
36. D. Graf *et al.*, *cond-mat/0312172* (2003).
37. D. Zanchi, A. Bjelis, and G. Montambaux, *Phys. Rev. B* **53**, 1240 (1996);
A. Bjelis, D. Zanchi and G. Montambaux, *J. Physique IV* **9**, 203 (1999).
38. E. Canadell, private communication.
39. M. Fujita, K. Machida and H. Nakanishi, *J. Phys. Soc. Jpn.* **54**, 3820 (1985).
40. W. Kang, S.T. Hannahs and P.M. Chaikin, *Phys. Rev. Lett.* **70**, 3091 (1993).
41. Y.J. Jo *et al.*, *Phys. Rev. B* **67**, 014516 (2003).
42. F. Wudl *et al.*, *J. Chem. Phys.* **76**, 5497 (1982).
43. R.C. Lacoé *et al.*, *Phys. Rev. B* **27**, 1947 (1983);
R.C. Lacoé *et al.*, *J. Physique Coll.* **44 C3**, 767 (1983).
44. F. Gross *et al.*, *Phys. Rev. B* **30**, 1282 (1984).
45. R. Moret *et al.*, *J. Physique Coll.* **44 C3**, 957 (1983).
46. R. Moret *et al.*, *Phys. Rev. Lett.* **49**, 1008 (1982);
C.S. Jacobsen *et al.*, *J. Phys.: Condens. Matter* **15**, 2651 (1982).
47. R. Moret *et al.*, *Phys. Rev. Lett.* **57**, 1915 (1986).
48. H. Schwenk *et al.*, *Phys. Rev. Lett.* **56**, 667 (1986);
W. Kang, J.R. Cooper and D. Jerome, *Phys. Rev. B* **43**, 11467 (1991).
49. O.H. Chung *et al.*, *J. Phys.: Condens. Matter* **15**, 7297 (2003).
50. V.M. Yakovenko, *J. Experimental and Theoretical Physics* **66**, 355 (1987).
51. D. Shoenberg, *Magnetic oscillations in Metals* (Cambridge University Press, 1984).
52. T. Osada *et al.*, *Phys. Rev. Lett.* **66**, 1525 (1991);
M.J. Naughton *et al.*, *Phys. Rev. Lett.* **67**, 3712 (1991);
W. Kang, S.T. Hannahs and P.M. Chaikin, *Phys. Rev. Lett.* **69**, 2827 (1992).
53. V.G. Peschansky, J.A.R. Lopez and T.G. Yao, *J. Physique I* **1**, 1469 (1991).
54. N. Hanasaki *et al.*, *Phys. Rev. B* **57**, 1336 (1998);
N. Hanasaki *et al.*, *Phys. Rev. Lett.* **60**, 11210 (1999).
55. M. Maesato *et al.*, *Rev. Sci. Instrum.* **71**, 176 (2000).
56. K. Murata *et al.*, *J. Phys. Chem. Solids* **63**, 1263 (2003).
57. S.Y. Han *et al.*, in *Physical Phenomena at High Magnetic Fields - III*, ed. L.G.Z. Fisk and J.R. Schrieffer (World Scientific, Tallahassee FL, 1998), p. 638-641.

58. C.E. Campos *et al.*, *Rev. Sci. Instrum.* **66**, 1061 (1995).
59. C.E. Campos *et al.*, *Phys. Rev. B* **53**, 12725 (1996).
60. J.S. Brooks *et al.*, *Synthetic Metals* **117**, 33 (2001).
61. P.M. Grant, *J. Physique Coll.* **44 C3**, 847 (1983).
62. G.M. Danner, W. Kang and P.M. Chaikin, *Phys. Rev. Lett.* **72**, 3714 (1994).
63. G.M. Danner and P.M. Chaikin, *Phys. Rev. Lett.* **75**, 4690 (1995).
64. E.I. Chashechkina and P.M. Chaikin, *Phys. Rev. Lett.* **80**, 2181 (1998).
65. D.G. Clarke *et al.*, *Science* **279**, 2071 (1998).
66. I.J. Lee, P.M. Chaikin and M.J. Naughton, *Phys. Rev. Lett.* **88**, 207002 (2002).
67. I.J. Lee *et al.*, *Phys. Rev. Lett.* **78**, 3555 (1997).
68. W.D. Wu *et al.*, *Synthetic Metals* **137**, 1305 (2003).
69. I.J. Lee *et al.*, *Phys. Rev. B* **68**, 092510 (2003).
70. J.I. Oh and M.J. Naughton, *Phys. Rev. Lett.* **92**, 067001 (2004).
71. S. Hill *et al.*, *Phys. Rev. B* **58**, 10778 (1998).
72. M.-S. Nam *et al.*, *Appl. Phys. Lett.* **83**, 4782 (2003).
73. S.S.P. Parkin, D. Jerome and K. Bechgaard, *Mol. Cryst. Liq. Cryst.* **79**, 213 (1981).
74. W.A. Little, *Phys. Rev.* **134**, A1416 (1964).
75. W.A. Little, *J. Physique Coll.* **44 C3**, 819 (1983).